Study of Ultraintense Laser-Produced Fast-Electron Propagation and Filamentation in Insulator and Metal Foil Targets by Optical Emission Diagnostics

M. Manclossi,[1,2] J. J. Santos,[1,3] D. Batani,[2,1,*] J. Faure,[1] A. Debayle,[3] V. T. Tikhonchuk,[3] and V. Malka[1]

[1]*Laboratoire d'Optique Appliquée, UMR 7639, ENSTA-CNRS-École Polytechnique, 91761 Palaiseau, France*

[2]*Dipartimento di fisica "G. Occhialini," Università degli studi di Milano-Bicocca, Milano, Italy*

[3]*Centre Lasers Intenses et Applications, UMR 5107, Université Bordeaux 1-CNRS-CEA, 33405 Talence, France*

(Received 9 December 2005; published 27 March 2006)

The transport of an intense electron beam produced by ultrahigh intensity laser pulses through metals and insulators has been studied by high resolution imaging of the optical emission from the targets. In metals, the emission is mainly due to coherent transition radiation, while in plastic, it is due to the Čerenkov effect and it is orders of magnitude larger. It is also observed that in the case of insulators the fast-electron beam undergoes strong filamentation and the number of filaments increases with the target thickness. This filamented behavior in insulators is due to the instability of the ionization front related to the electric field ionization process. The filamentary structures characteristic growth rate and characteristic transversal scale are in agreement with analytical predictions.

DOI: 10.1103/PhysRevLett.96.125002 PACS numbers: 52.57.Kk, 52.38.Kd, 52.38.Hb, 52.70.Kz

The understanding of the transport of fast electrons through dense matter is of crucial importance for both the fast ignition (FI) scheme of the inertial confinement fusion and the optimization of laser-driven proton sources [1]. In the FI concept, the ignition of a precompressed pellet containing the fusion fuel is initiated by laser-produced electrons with energies in the MeV range [2]. It is crucial for this scheme that the energy of the ignitor laser be efficiently converted into an intense electron beam that can propagate through the high density overcritical plasma and initiate the thermonuclear burn in the core [3]. The transport of the electrons to the precompressed core involves currents of the order of 100–1000 MA which largely exceeds the Alfvén limit. Their propagation is possible only if return currents formed by the background electrons of the material balance the incoming fast-electron current and cancel the charge separation. However, under these conditions (two counterstreaming intense currents), kinetic instabilities such as two-stream or Weibel-like instabilities [4,5] may develop and particle-in-cell simulations predict that the transport of the relativistic electron beam leads to filamentation.

In this context, a number of experiments investigating the propagation and filamentation of laser-produced relativistic electron beams have been performed using metal and plastic foils, foam targets, and glass slabs [6–9].

Filamentary structures have been reported in [8], but their observation was very indirect, far from the target, where propagation and filamentation take place. The filaments and electron jets have been directly observed in [6,10] but only in insulator targets. From these data, it is not possible to conclude whether the filamentation is due to a volumic mechanism (like two-stream or Weibel instability) or whether it is connected to the ionization instability taking place at the electron beam front. Moreover, no parametric study has been performed by systematically changing target and/or laser parameters.

In insulators, the charge separation at the edge of the propagating intense electron beam produces a strong electrostatic field [11,12], which very rapidly ionizes the material. Free electrons are then set in motion and they establish a return current. Thus, effectively, the bulk of the fast-electron beam propagates in a dense plasma, the conductivity of which is only marginally different from the conductivity of a metal. However, according to [13], the ionization front becomes unstable because its velocity increases with the electron beam local density. This enhances small corrugations of the ionization front which grow in time. Therefore, if the Weibel instability is the dominant filamentation process, it should act in a similar way in insulators and conductors. On the contrary, a ionization instability takes place only at the fast beam edge (ionization front) during the electron beam propagation through an insulator.

Another important point is the detection of such instabilities. Recently, optical transition radiation (OTR) and coherent transition radiation (CTR) diagnostics have been largely used for direct observation of fast-electron transport [9,14–16]. However, in transparent dielectrics one should also take into account Čerenkov emission [17]. Čerenkov light can be emitted by fast electrons from the ionization front only, because the ionized plasma is not transparent and it has a small refraction index $n \lesssim 1$. Thus, a diagnostic based on Čerenkov emission is naturally adapted for detecting ionization instabilities in dielectrics.

In this Letter, we present a detailed study of fast-electron propagation through insulators and conductors, performed by using the target rear side optical radiation as a diagnostic tool. We show that in the case of plastic targets the optical emission is several orders of magnitude greater than in metals. The target rear side emission has been imaged with high spatial resolution, clearly demonstrating a uniform fast-electron propagation in conductors and a beam filamentation in dielectrics. The transverse scale length and

the growth rate of this instability are in good agreement with analytical predictions based on a model of electric field ionization and ionization front instability.

The experiment was performed on the ''salle jaune'' Ti:Sapphire laser at Laboratoire d'Optique Appliquée (LOA), which operates in the chirped-pulse amplification mode at the wavelength of 815 nm [18]. The laser delivers 40 fs (FWHM) pulses with on-target energies up to 0.7 J. The laser beam was focused with a $f/5$ off-axis parabolic mirror at normal incidence onto thin foils of aluminum (Al) or plastic (CH) with thicknesses ranging from 10 to 100 μm. The waist of the focal spot was 6 μm, resulting in focused intensities in vacuum of the order of 6×10^{19} W/cm^2, and a contrast ratio better than 10^{-6}.

The target rear side was imaged on axis by means of a $\sim f/2$ optical system on a ($256 \times 1024 - 16$ bit) CCD or on an intensified ($1024 \times 1024 - 16$ bit) CCD (ICCD) camera as shown in Fig. 1, configurations (A) and (B). These cameras were adequately filtered using BG38 and BG39 filters to suppress the undesirable 815 nm light from the laser beam. In some shots, the spectral window of the camera was limited to a bandwidth of 10 or 90 nm around two wavelengths [405 ± 5 nm and 546 ± 5 nm for configuration (A); 430 ± 37 nm and 525 ± 45 nm for configuration (B)] by using narrow-band filters. The sensitivity of the imaging system was obtained with an absolutely calibrated blackbody radiation lamp. The spatial resolution of the system was $\lesssim 5$ μm.

The measurements of the optical emission for aluminum and plastic targets vs thickness L are presented in Fig. 2 for two spectral bands: around 405 and 546 nm. These spatially resolved and time-integrated (over 5 ns) results where obtained with full energy shots ($\sim$0.7 J on target) and narrow-band interferometric filters ($\Delta\lambda \sim 10$ nm) coupled with an ICCD camera [see Fig. 1, configuration (A)]. The signals (total collected energy per spectral increment) at both wavelengths are about 100 times more intense in CH than in Al. Also, apart from the range of the thin targets ($L < 50$ μm), for growing thickness both signals decrease in Al (the 546 nm signal faster than the 405 nm signal) and increase in CH (with no remarkable difference between the 546 and the 405 nm signals).

In our experiment, the interaction laser pulse was preceded by a $\sim$3 ns amplified spontaneous emission (ASE) pedestal with an intensity contrast better than 10^{-6}. The effects of such a long and intense prepulse have been estimated in hydrodynamic simulations performed with the hydrodynamic code MULTI-1D [19,20]. We found that this ASE level is sufficient to evaporate ~ 2 μm of material and to generate a shock wave with a pressure of $\sim$1.6 Mbar [21]. After the shock breakout, the target might be accelerated and displaced to a distance of a few tens of μm depending on the thickness. In particular, the thinnest 13 μm CH foils may move to about 40 μm (to be compared with the $\sim$100 μm focal depth of the laser beam) before the arrival of the main pulse. Such a motion might change the interaction conditions for thin targets but it should not affect the foils thicker than $\sim$30 μm where no shock breakout from rear side is possible before the main pulse arrival.

Concerning the intensity of the optical emission observed in Fig. 2, three mechanisms have to be considered: (i) the transition radiation, i.e., the light emitted by electrons crossing the rear target boundary, (ii) the thermal emission from the rear target surface, and (iii) the Čerenkov radiation.

Our analysis shows that the first two mechanisms can explain the signal from Al targets. For thick targets ($\gtrsim 30$ μm for signals around 405 nm and $\gtrsim 75$ μm for signals around 546 nm, respectively, black and gray circles in Fig. 2) the emission is dominated by CTR produced by a microbunched relativistic tail of the fast-electron distribution and its intensity decreases with the target thickness. The emission from the Al thinner targets ($\lesssim 30$ μm and $\lesssim 75$ μm, respectively) is mainly due to the second mechanism—the blackbody radiation emitted in consequence of the heating induced by the ASE-induced shock wave and the return electron current balancing the current of fast electrons. By summing the contribution of these two mechanisms, one

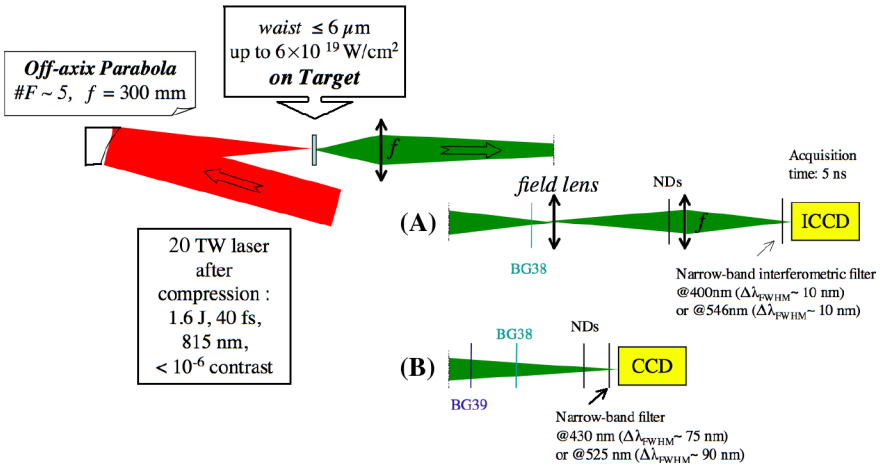

FIG. 1 (color online). Experimental setup. Configuration (A) ICCD image system; configuration (B) CCD imaging. NDs stands for neutral densities.

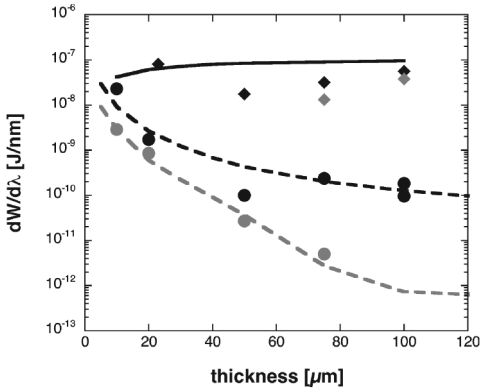

FIG. 2. Data series for Al (circles) and CH (diamonds) targets for the laser intensity 6×10^{19} W/cm^2. Black symbols stand for the signals around 405 nm and the gray symbols for the signals around 546 nm. Aluminum data are completely fitted by the sum contribution of CTR and thermal emission (dashed curves). For the CH targets, one has to add the Čerenkov radiation and the total emission from all radiative contributions fits correctly the CH data (solid curve).

can explain all Al data as can be seen in Fig. 2. However, these processes cannot describe the CH data where the optical signal increases with the target thickness. Such behavior can be explained only by the Čerenkov emission, which is proportional to the particle path length and therefore to the target thickness.

In some shots, the front side of the CH targets was covered by a thin (~30 nm) Al layer. However, this does not change the results, showing that the larger signal from the plastic target is not due to a change in the laser interaction conditions on the front side. Furthermore, in order to check that this increased signal intensity is not due to OTR and to the difference in the refraction index between CH and Al, some plastic targets were shot with the thin Al (~30 nm) layer on the rear side. The signals recorded with these targets show a decrease but were still higher than the OTR signals from Al targets. The decrease in signal fits with the small absorption in the Al layer. Other than that, the results were not affected, confirming that the signal comes from Čerenkov radiation in plastic.

The optical Čerenkov radiation is emitted by an electron propagating in a dielectric material with a velocity $v = \beta c$ larger than the light phase velocity c/n [22]. However, it cannot be observed in nontransparent materials such as metals or dense plasmas because of strong absorption and a small refraction index $n < 1$. The radiation is emitted in a cone around the particle propagation axis with an angle given by $\cos\theta = 1/\beta n$. Given the $\sim f/2$ collection optics and the CH refractive index in the 400–550 nm wavelength range ($n \sim 1.48$), we can observe emission only in the narrow cone within $\theta_{\max} \approx 8°$ around the target normal.

Another important limitation on the Čerenkov emission is imposed by the ionization process: the detected radiation is due to relatively high energy electrons ($\beta \sim 0.85$–0.95) propagating with the head of the ionization front at large angles $\gtrsim$ 30–40° (with respect to the target normal). This is because (i) only electrons with velocities larger than the ionization front ($\beta > \beta_f$) can contribute to the measured signal, and (ii) electrons moving along the laser axis emit radiation which is outside the collection angle.

The ionization of CH targets is triggered by the fastest electrons, which travel at velocities faster than the ionization front velocity $v_f = \beta_f c$ and create the charge separation electric field which ionizes the neutral atoms. Estimates [11,13] show that the electric field at the ionization front is of the order of 10% of the atomic electric field E_a and that about 10% of fast electrons participate in the ionization process. Then, one can roughly estimate the width of the ionization front from the Poisson equation as $\Delta_f \sim \epsilon_0 E_a / e n_b \sim 1$–$2$ μm. This length is about one-tenth of the beam length, $l_b \sim c\tau \sim 10$ μm, where τ is the laser pulse duration, which is another way to estimate the relative number of electrons participating in the ionization process.

According to previous results [9,23], the fast-electron population is assumed to have a relativistic Maxwellian energy distribution with the temperature $T_h \simeq 1$ MeV, a Gaussian angular distribution with an angular divergence ~30° around the laser axis, and a total number of particles $N_b = 2 \times 10^{12}$ injected in a $r_0 \approx 15$ μm radius surface. The initial density of the electron beam is of the order of $n_b \sim 2.4 \times 10^{20}$ cm^{-3} and it decreases by 1 order of magnitude at the rear side of a 100 μm thickness target as the beam radius r_f increases to a final value of ~70 μm.

The characteristics of the Čerenkov emission have been revisited recently in Ref. [24]. It should be largely coherent because the ionization front thickness Δ_f is comparable to the emission wavelength. The radiation intensity was estimated from the following equation [24]:

$$\frac{d^2W}{dz d\lambda} \approx \Delta\Omega \frac{e^2 N_b^2 \sin^2\theta}{\epsilon_0 \lambda^3 \cos\theta} e^{-(k r_f \tan\theta)^2} \delta(1 - \beta n \cos\theta),$$

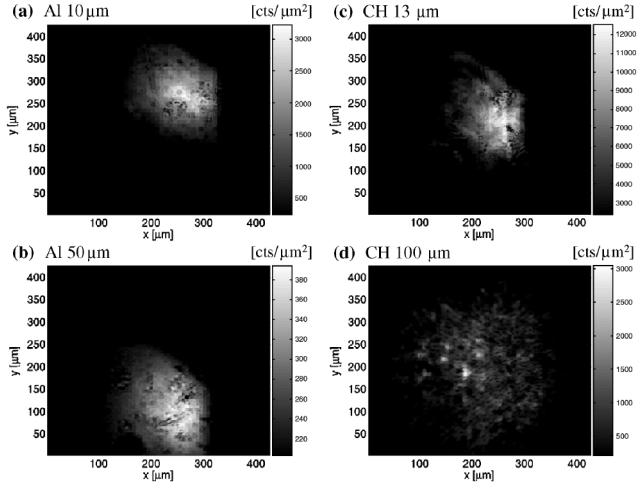

FIG. 3. Optical emission (counts/μm^2) images obtained using 10 and 50 μm Al [(a),(b)] and 12, 100 μm CH targets [(c),(d)].

where $\Delta\Omega \simeq \pi\theta_{\max}^2$ is the acquisition solid angle, $k = 2\pi n/\lambda$, N_b is the total number of electrons, and the exponential factor accounts for the coherence length in the front plane. This equation was averaged over the electron propagation directions and over the electron energies (only for $\beta > \beta_f$) and integrated over the target. The results are presented in Fig. 2. Because of the limitations discussed above, only a few percent of electrons contribute to the Čerenkov emission. However, it is indeed the dominant radiation mechanism and it fairly well reproduces the CH data.

We also performed a detailed study of the spatial distribution of the rear side target emission. A series of typical optical images are shown in Fig. 3 for ~0.45 J laser energy on Al and CH targets with thicknesses varying from 10 to 100 μm. A spectral region around 525 nm was selected using a $\Delta\lambda \sim 90$ nm GG495 SCHOTT filter [see Fig. 1, configuration (B)].

Concerning the thin targets, one observes a similarity between Fig. 3(a) (Al) and Fig. 3(c) (CH). This is related to the fact that those targets were strongly perturbed by the ASE before the main pulse arrival creating similar conditions in both materials for the generation and transport of fast electrons.

A significant difference between conductors and insulators can be seen for targets thicker than 30 μm. As expected in Al targets, the signal is spatially homogeneous. There is only a moderate increase in beam size and reduction in signal for larger thicknesses. On the contrary, in the CH targets, the electron beam is split into filaments [Fig. 3(d)] with sizes of ~13 μm. According to analytical predictions [13], this beam filamentation can be related to the corrugation instability of the ionization front. The ionization front is unstable and it splits into filaments because the velocity of the ionization front increases with the electron beam density. Indeed, a small increase in the electron beam density accelerates the ionization and advances further the ionization front. This further increases the electron concentration and provokes the beam splitting into filaments. The instability growth rate maximum corresponds to the wavelengths of the order of the front thickness, $\lambda_c \sim 2\pi\Delta_f$. This estimates agrees with the experimentally observed size of filaments. The predicted instability growth rate $\Gamma_c \sim 10^{13}$ s^{-1} corresponds to a beam filamentation distance of about ~100 μm which is of the same order as that observed experimentally [Fig. 3(d)]. This maximum growth rate is achieved for the current density ~100 A/μm^2, which agrees rather well with the estimate of 7 MA for the total current in our experiment. This is in agreement with the current estimates in other experiments [9,23]. On the contrary, producing filaments on the distance of 100 μm with the dissipative Weibel instability would require current densities above 1 kA/μm^2, which are not realistic in our conditions. Let us also note that, assuming a filament size of ~13 μm (as measured in the experiment), one would get ~40 kA of current per filament, which is quite close to the Alfvén limit.

In conclusion, we have studied the propagation of fast electrons through conductor and insulator targets, showing beam filamentation in plastic. The optical emission from the target rear side is ascribed to coherent transition radiation and to thermal emission for Al targets [25], while for CH targets Čerenkov emission is the dominant mechanism. The Čerenkov diagnostic clearly shows that the electron beam breaks up into filaments with a growth rate and a characteristic transversal scale in fair agreement with analytical predictions based on the ionization front instability. This large scale (~10 μm) and relatively slow ($\Gamma_c \sim 10^{13}$ s^{-1}) filamented behavior is completely absent in metals, and therefore it cannot be explained with a volumic instability such as the Weibel or two-stream instabilities.

We gratefully acknowledge the assistance of the LOA laser and technical staff as well as S. Krasheninnikov for fruitful discussions. The authors also thank O. Bernard from Andor Technology for lending an ICCD camera.

*Electronic address: batani@mib.infn.it

[1] M. Roth *et al.*, Phys. Rev. ST Accel. Beams **5**, 061301 (2002).
[2] M. Tabak *et al.*, Phys. Plasmas **1**, 1626 (1994).
[3] C. Deutsch *et al.*, Phys. Rev. Lett. **77**, 2483 (1996).
[4] E. S. Weibel, Phys. Rev. Lett. **2**, 83 (1959).
[5] F. Califano *et al.*, Phys. Plasmas **9**, 451 (2002).
[6] M. Borghesi *et al.*, Phys. Rev. Lett. **83**, 4309 (1999); L. Gremillet *et al.*, Phys. Rev. Lett. **83**, 5015 (1999); M. Tatarakis *et al.*, Phys. Rev. Lett. **90**, 175001 (2003).
[7] J. Fuchs *et al.*, Phys. Rev. Lett. **91**, 255002 (2003); T. A. Hall *et al.*, Phys. Rev. Lett. **81**, 1003 (1998); H. Teng *et al.*, Phys. Rev. E **67**, 026408 (2003).
[8] M. S. Wei *et al.*, Phys. Rev. E **70**, 056412 (2004).
[9] J. J. Santos *et al.*, Phys. Rev. Lett. **89**, 025001 (2002).
[10] D. Batani *et al.*, Phys. Rev. Lett. **94**, 055004 (2005).
[11] V. T. Tikhonchuk, Phys. Plasmas **9**, 1416 (2002).
[12] J. R. Davies, Phys. Rev. E **68**, 056404 (2003).
[13] S. I. Krasheninnikov *et al.*, Phys. Plasmas **12**, 073105 (2005).
[14] S. D. Baton *et al.*, Phys. Rev. Lett. **91**, 105001 (2003).
[15] J. Zheng *et al.*, Phys. Rev. Lett. **92**, 165001 (2004).
[16] H. Popescu *et al.*, Phys. Plasmas **12**, 063106 (2005).
[17] F. Brandl *et al.*, Europhys. Lett. **61**, 632 (2003).
[18] M. Pittman *et al.*, Appl. Phys. B **74**, 529 (2002).
[19] R. Ramis *et al.*, Comput. Phys. Commun. **49**, 475 (1988).
[20] K. Eidmann *et al.*, Phys. Rev. E **62**, 1202 (2000).
[21] D. Batani *et al.*, Phys. Rev. E **68**, 067403 (2003).
[22] L. D. Landau and E. M. Lifshitz, *Electrodynamics of Continuous Media* (Pergamon, Oxford, 1984), 2nd ed.
[23] K. B. Wharton *et al.*, Phys. Rev. Lett. **81**, 822 (1998).
[24] J. Zheng *et al.*, Phys. Plasmas **12**, 093105 (2005).
[25] J. J. Santos *et al.* (to be published).